Applied Catalysis B: Environmental 185 (2016) 315–321

Contents lists available at ScienceDirect

Applied Catalysis B: Environmental

journal homepage: www.elsevier.com/locate/apcatb

Holey structured graphitic carbon nitride thin sheets with edge oxygen doping via photo-Fenton reaction with enhanced photocatalytic activity

ShuaiNan Guo, Yong Zhu, YunYun Yan, YuLin Min*, JinChen Fan*, QunJie Xu*

Shanghai Key Laboratory of Materials Protection and Advanced Materials in Electric Power, Shanghai University of Electric Power, 200090, China

ARTICLE INFO

Article history:
Received 20 June 2015
Received in revised form
21 September 2015
Accepted 20 November 2015
Available online 24 November 2015

Keywords:
Graphitic carbon nitride
Photocatalytic activity

ABSTRACT

Holey structured graphitic carbon nitride thin sheets with edge oxygen doping (HS g-C_3N_4-O) via photo-Fenton reaction were reported. The HS g-C_3N_4-O exhibited high surface area of 348 m^2 g^{-1} and narrow bandgap (2.434 eV), hence producing high photocatalytic activities for both H_2 generation and Rh.B degradation under solar light irradiation.

1. Introduction

Photocatalytic hydrogen generation from water using photo-driven reaction has attracted considerable attention as an ideal green technology [1–3]. Of these, a stable photocatalysts which high effectively converts solar energy into chemical fuels is an appreciated alternative. Among various semiconductors photocatalyst, metal-free graphitic carbon nitride (g-C_3N_4) with a suitable band gap and edges has emerged as a new class of photocatalyst due to its nontoxicity, thermal and chemical stability. However, the latest documented quantum yields for H_2 production using pristine g-C_3N_4 does not exceed 4% [4–7], which is far from satisfactory for further application.

As is known, an excellent photocatalyst must possess a high specific surface area to take place redox reactions and a minimizing recombination to take advantage photo-induced charge. Undeniably, the bulk g-C_3N_4 has poor surface area and the high recombination rate. To improve the essential properties of g-C_3N_4, various strategies including heteroatom doping [8–11], layer exfoliation [12], heterojunction configuration [12–15] and carbonaceous scaffold [16–18] have been adopted. Meanwhile, Oxygen heteroatom has been successfully introduced by a simple H_2O_2 oxidation and its photoactivity has been improved to some extent [19,20]. However, the strongly oxidizing agent of H_2O_2 would be easily break the g-C_3N_4 structure whose is possibly converted into carbon or nitrite oxides. In this sense, rationally controlling the oxidation process would leave behind many vacancies, which could be gradually extended into nanopores texture. The expected oxygen doped g-C_3N_4 with high porosity is able to exhibit impressive photocatalytic activity due to simultaneous doping effect and high active sites.

In this study, a holey structured g-C_3N_4 with edge oxygen doping (HS g-C_3N_4-O) was successfully obtained using photo-Fenton reaction in presence of Fe^{3+}/Fe^{2+} and H_2O_2. First, bulk g-C_3N_4 was oxidized and exfoliated into g-C_3N_4 thin sheets with abundant oxygen-containing groups, which based on Niu et al. report [12]. Furthermore, it has also been demonstrated that the photo-Fenton reaction can generate hydroxyl radicals ($OH^{\bullet}$) under the photoassisted catalysis of Fe^{3+}/Fe^{2+} in present of H_2O_2, and which has been considered as one of the most powerful oxidizing species [21]. Thus, the g-C_3N_4 thin sheets with abundant oxygen-containing groups as active defective sites can be partially oxidized and etched, leaving behind carbon vacancies, which gradually extend into nanopores [22,23]. The as-resulted HS g-C_3N_4-O demonstrated a narrow bandgap of 2.434 eV and high surface area of 348 m^2 g^{-1}, thus presenting highly efficient photocatalytic activity for H_2 generation and Rh.B degradation.

* Corresponding authors.
E-mail addresses: ahaqmylin@126.com (Y. Min), jinchen.fan@gmail.com (J. Fan), xuqunjie@shiep.edu.cn (Q. Xu).

http://dx.doi.org/10.1016/j.apcatb.2015.11.030
0926-3373/

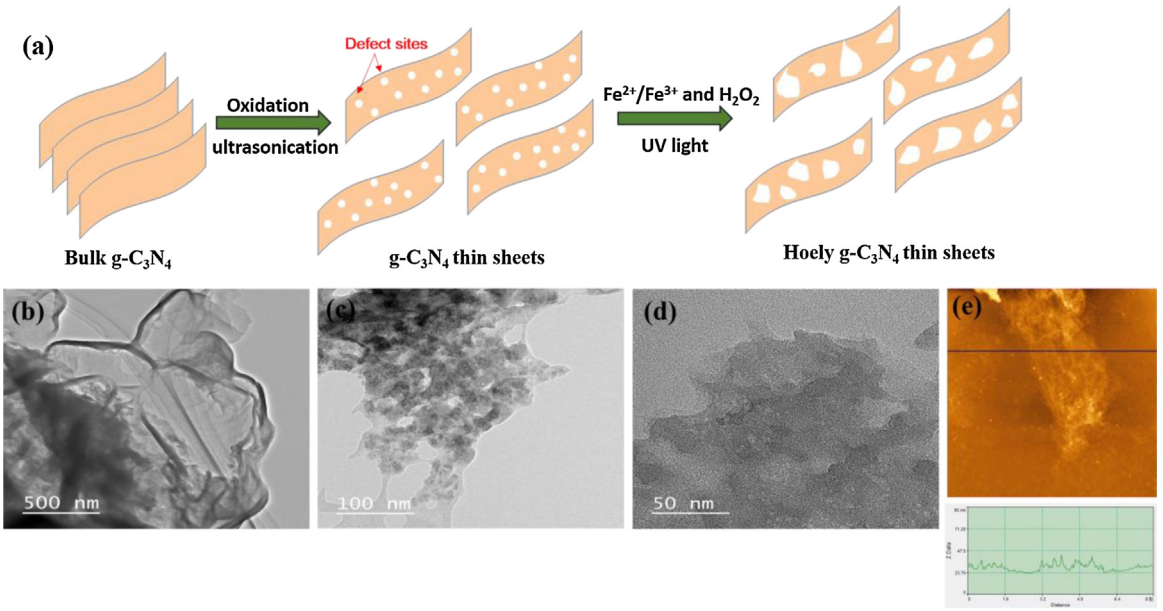

Fig. 1. (a) Schematic illustration of the HS g-C_3N_4-O formation via photo-Fenton reaction. (b) TEM image of oxidized g-C_3N_4 thin sheets. (c and d) TEM image of the HS g-C_3N_4-O. (e) AFM image of the HS g-C_3N_4-O.

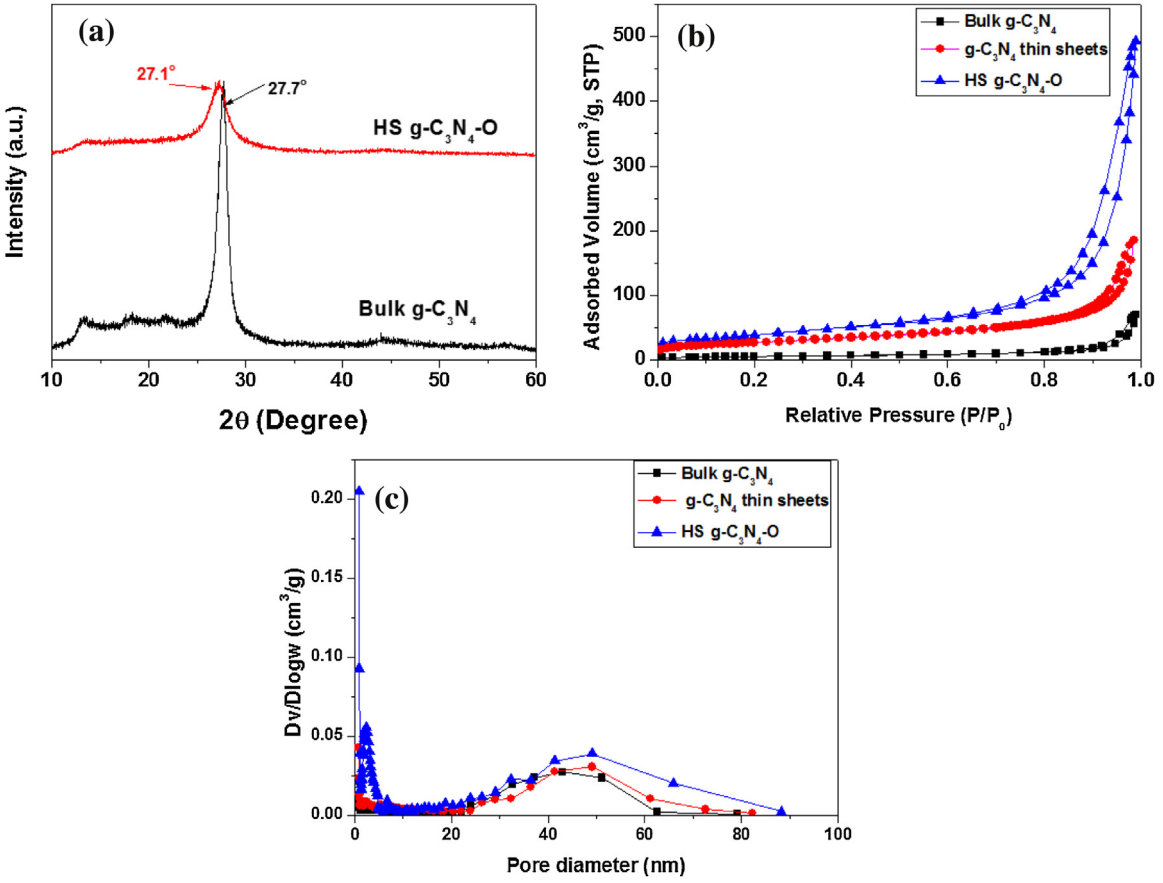

Fig. 2. (a) XRD patterns of the bulk g-C_3N_4 and HS g-C_3N_4-O. (b) Nitrogen adsorption–desorption isotherms and the corresponding pore size distribution curves (c) of the bulk g-C_3N_4, g-C_3N_4 thin sheets and HS g-C_3N_4-O.

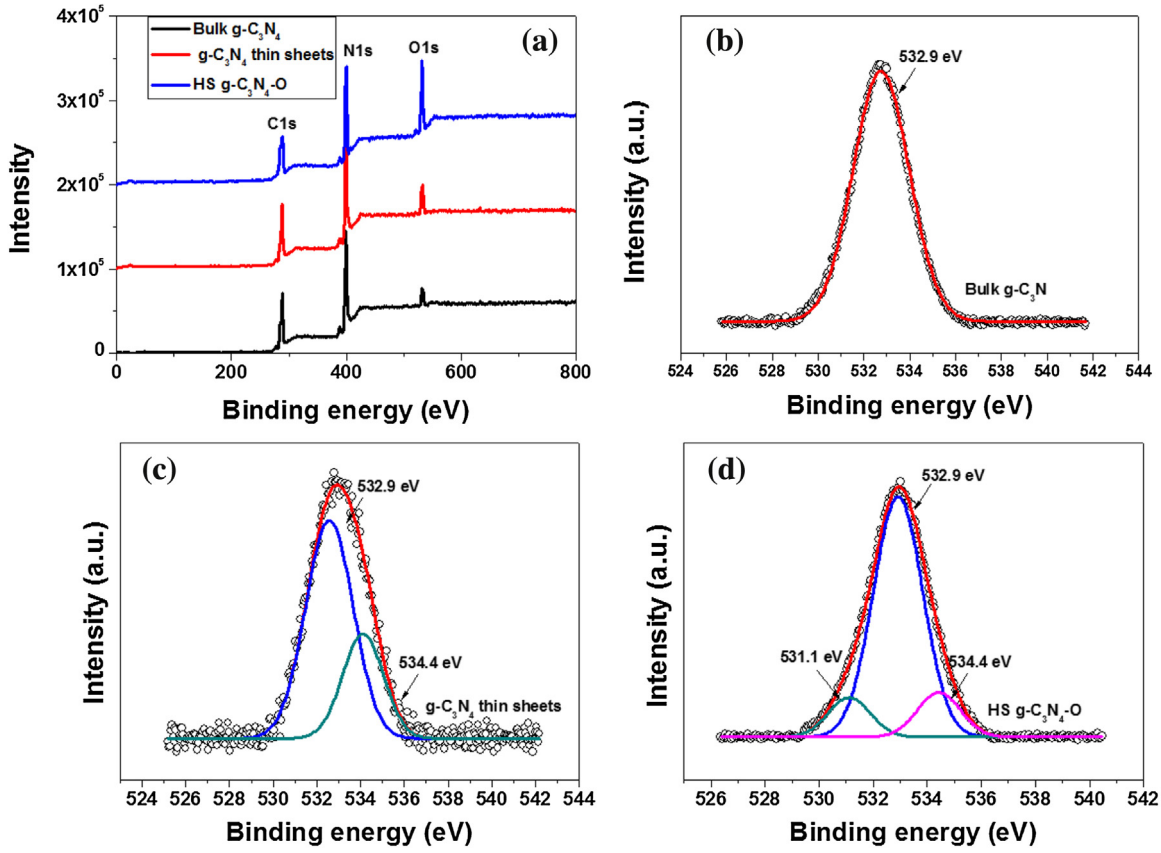

Fig. 3. (a) Full XPS spectra of the bulk g-C_3N_4, g-C_3N_4 thin sheets and HS g-C_3N_4-O. (b) High resolution O1s XPS spectra of the bulk g-C_3N_4. (c) High resolution O1s XPS spectra of the g-C_3N_4 thin sheets. (d) High resolution O1s XPS spectra of HS g-C_3N_4-O.

2. Experimental

2.1. Materials

Rhodamine B, H_2SO_4, HNO_3, H_2O_2 were purchased from Shanghai Pure Chemical Co., Ltd., China. Other materials were obtained from Sigma–Aldrich.

2.2. Synthesis of HS g-C_3N_4-O

Bulk g-C_3N_4 was synthesized by directly heating melamine in the semiclosed system to prevent the sublimation of melamine at 550 °C for 4 h. First, 1 g of bulk g-C_3N_4 was treated in the mixture of concentrated H_2SO_4 and HNO_3 with 1:1 volume ratio for about 2 h at room temperature. The mixture was then diluted with deionized water (1 L) and washed for several times, the as-obtained white product was g-C_3N_4 thin sheets. The photo-Fenton reactions of g-C_3N_4 thin sheets were carried out under UV light irradiation (λ = 365 nm). The reaction is carried out under vigorous stirring in a 40 mL quartz tube which is installed 5 cm away from the irradiation lamp. In a typical experiment, 0.5 mg g-C_3N_4 thin sheets were dispersed in 5 mL water, then, 20 mL of 20 mM H_2O_2, and 100 μL of 1.0 mM of $FeCl_3$ were added. The pH of the mixture was adjusted to 4. The reaction was maintained around 5 h under continuous irradiation of UV light. The reaction products were washed with 0.1 mmol HCl and deionized water several time to remove residual iron ions until the pH 7. The HS g-C_3N_4-O was collected by centrifugation and dried at 60 °C.

2.3. Analysis instruments

The N_2 adsorption isotherm was measured at 77 K using a BEL sorp Analyzer (BEL, Japan). The XRD patterns were obtained with a diffractometer on Riguka, Japan, RINT 2500 V using Cu Kα radiation. The Fourier transform-infrared (FT-IR) spectra were recorded in KBr pellets with a Bruker FT-IR. The diffuse reflectance UV–vis absorption spectra were obtained using a spectrophotometer (Shimadzu UV-2401PC) equipped with a diffuse reflectance accessory, and $BaSO_4$ was used as the reference. Transmission electron microscopy (TEM) observations were obtained using a JEM-2200FS microscope with Cs correction. The photoluminescence of the powder samples was recorded at room temperature using a fluorescence spectrometer (Shimadzu UV-2401PC). The UV–vis absorption spectra were recorded using a (S-3100, Sainco. Co., Ltd.) spectrometer.

2.4. Photoelectrochemical measurements

Photocurrent responses were carried out in a conventional three-electrode system using a potentiostat (CH Instruments, CHI 660). The photocurrents were collected and measured via electron shuttles on an inert Pt electrode immersed in the 0.5 M Na_2SO_4 solution at 0.2 V potential bias under a solar simulator with Xe lamp through a UV-cutoff filter (>420 nm) served as a light source. The electrodes was prepared by dropping 20 μL aqueous slurry that consisted of 50 mg of prepared sample with 200 μL of H_2O, 5 μL of acetylacetone, and 5 μL of Nafion on a cleaned ITO glass substrate. After air dried, the electrode was annealed at 300 °C for

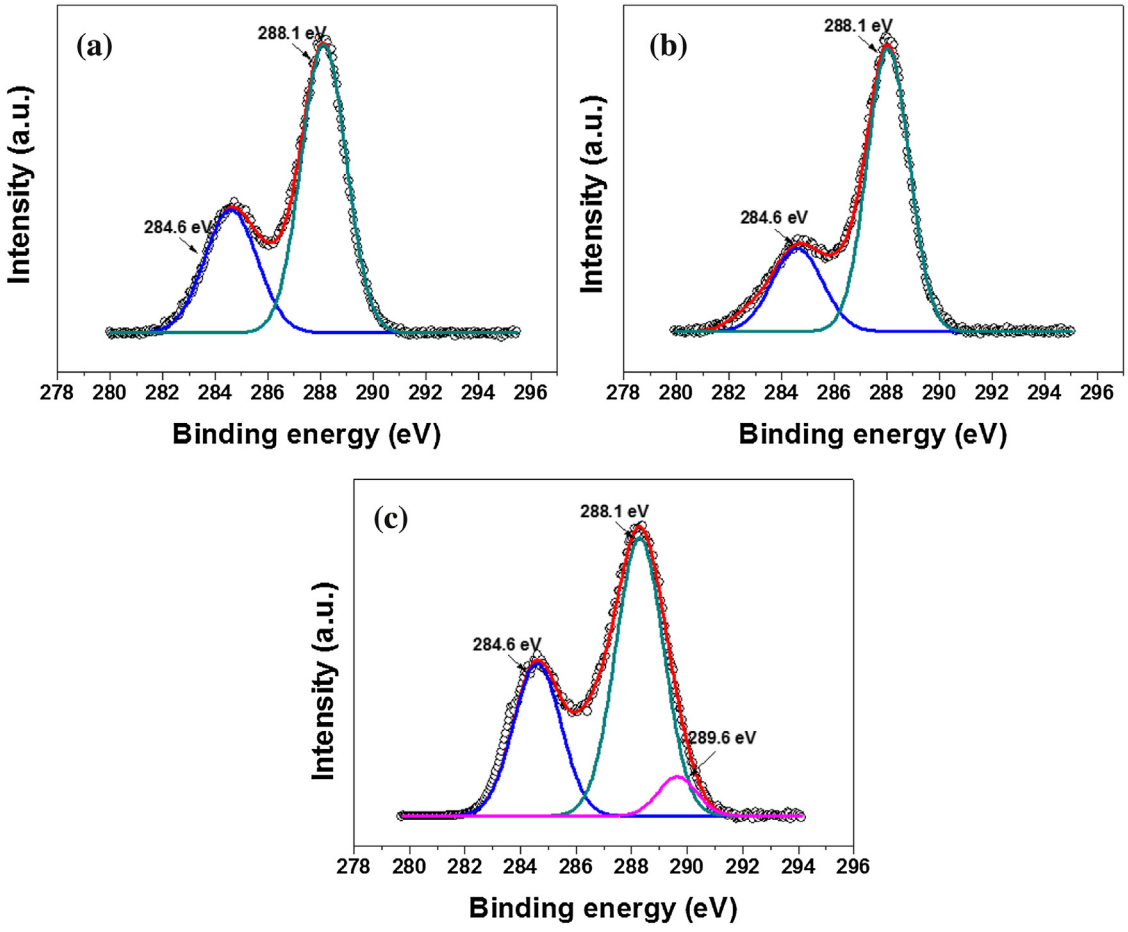

Fig. 4. (a) High resolution C1s XPS spectra of the bulk g-C_3N_4. (b) High resolution C1s XPS spectra of the g-C_3N_4 thin sheets. (d) High resolution C1s XPS spectra of HS g-C_3N_4-O.

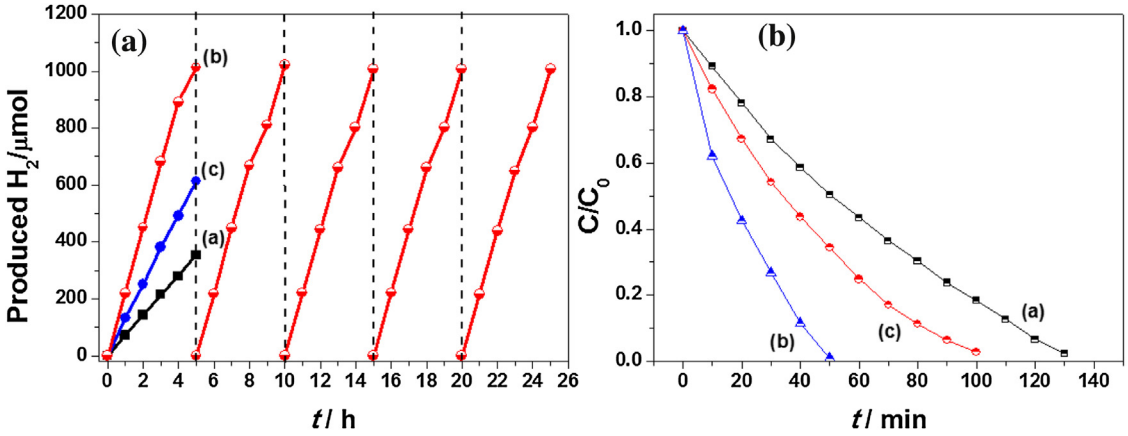

Fig. 5. (a) Photocatalytic activities toward H_2 production of (a) bulk g-C_3N_4, (b) HS g-C_3N_4-O and (c) g-C_3N_4 thin sheets under visible light irradiation. (b) Photocatalytic activities toward Rh.B decolorization of (a) bulk g-C_3N_4, (b) HS g-C_3N_4-O and (c) g-C_3N_4 thin sheets under visible light irradiation.

2 h in air. Mott–Schottky tests was performed with the potentials ranged from −0.5 V to 1 V (vs Ag/AgCl) at the selected frequencies of 1.5 kHz.

2.5. Photocatalytic test

For photodegradation of organic dyes, the decomposition reaction of a 50 mL Rh.B (2×10^{-5} M) aqueous solution was carried out. A powdered sample of 30 mg was dispersed in the Rh.B solution under ultrasonication for 1 min, and then was kept in dark conditions for 1.5 h. For the irradiation system, a 300 W Xe lamp with 420 nm filter was used at the distance of 100 mm from the solution in a darkness box. The suspension was irradiated for different irradiation times. The samples were then withdrawn regularly from the reactor and the dispersed powder was removed through centrifugation. The clean transparent solution was analyzed by UV–vis spectroscopy. The concentration of Rh.B in the solution was determined as a function of irradiation time from the absorbance

Table 1
BET surface area, total pore volume and average pore size of bulk g-C_3N_4, g-C_3N_4 thin sheet and HS g-C_3N_4-O.

Item	Bulk g-C_3N_4	g-C_3N_4 thin sheet	HS g-C_3N_4-O
S_{BET} ($m^2\ g^{-1}$)	46	106	348
V_{total} ($cm^3\ g^{-1}$)	0.041	0.075	0.155
D (nm)	12.8	13.2	17.6

region at a functional wavelength. Photocatalytic hydrogen evolution was carried out in a Pyrex top-irradiation reaction vessel connected to a closed glass gas system. In detail, 30 mg of catalyst powders was dispersed in the aqueous solution (200 mL) containing triethanolamine (20 vol.%) as sacrificial agent. Co-catalysts Pt nanoparticles were introduced by in-situ photodeposition method as reported before, where loaded amount of Pt was estimated to be about 5 wt.%. 1 mL sample of the generated gas was collected using a glass injection syringe which could be sealed up and the hydrogen and oxygen contents were analyzed using a gas chromatograph.

3. Results and discussion

The formation processes of HS g-C_3N_4-O is schematically shown in Fig. 1a. The SEM images of the bulk g-C_3N_4 and oxidized g-C_3N_4 thin sheets are shown in Fig. S1. The TEM image of oxidized g-C_3N_4 thin sheets was exhibited in Fig. 1b, demonstrating a surface rough sheet with large area. Furthermore, the oxidized g-C_3N_4 thin sheets have a tendency to edge bend due to minimizing the Van der Waals' force and surface energy [12]. Fig. 1c and d indicates that the etching process could occur across the entire g-C_3N_4 thin sheets to result in abundant in-plane pores of a few nanometers, demonstrating holey structured g-C_3N_4 thin sheets. AFM image of the holey structured g-C_3N_4 thin sheets appears as loose and soft agglomerates with a size of tens of micrometers (Fig. 1e). The compared with the pristine g-C_3N_4, the crystallinities of HS g-C_3N_4-O are weakened at ~13°, corresponding to a weak interplanar structure. The (0 0 2) peak of HS g-C_3N_4-O slightly shifted toward low angle, indicating a more loose of C—N planes due to oxygen doping (Fig. 2a). The effects of holey structure on the BET surface area and porous structures of g-C_3N_4 thin sheets were investigated using adsorption–desorption measurements. As shown in Fig. 2b, the remarkable hysteresis loops indicate the mesoporous nature (2–50 nm) of these g-C_3N_4 and their derivatives. Moreover, the adsorption branch of nitrogen isotherms shows a steady increase at P/P_0 approaching unity, suggesting the formation of large mesopores and small macropores. The pore size distributions of bulk g-C_3N_4, g-C_3N_4 thin sheets and HS g-C_3N_4-O are shown in Fig. 2c. The pore-size distributions are very broad, indicating the existence of mesopores and macropores. Particularly, the HS g-C_3N_4-O shows a more prominent pore size distribution in the range of 1–5 nm, which could be ascribed to the nanopores in the basal plane of HS g-C_3N_4-O, which is consistent with TEM analysis. The porous properties of these materials are summarized in Table 1, including the specific surface area (S_{BET}), total pore volume, and average pore diameter. It is clearly seen that the S_{BET} of both g-C_3N_4 thin sheets (106 $m^2\ g^{-1}$) and HS g-C_3N_4-O (348 $m^2\ g^{-1}$) is higher than that of bulk g-C_3N_4 (46 $m^2\ g^{-1}$), respectively. A greater specific surface area of photocatalysts can supply more surface active sites and make charge carriers transport easier, leading to an enhancement of the photocatalytic performance [24].

X-ray photoelectron spectroscopy (XPS) was employed to confirm oxygen doping species in HS g-C_3N_4-O. Besides the appearance of expected C and N elements, comparison full XPS spectra among bulk g-C_3N_4, g-C_3N_4 thin sheets and HS g-C_3N_4-O clearly reveals that significant content of oxygen is doped in HS g-C_3N_4-O (Fig. 3a). Their high-resolution O1s XPS spectra show core level at 532.9 eV, which is ascribed to adsorbed water (Fig. 3b–d) [25]. It is understandable the intensity increase in HS g-C_3N_4-O because the HS g-C_3N_4-O has much high surface area, leading to numerous water adsorbed on surface. Furthermore, the deconvolution of O1s XPS exhibited two additional peaks at 531.1 and 534.4 eV in the HS g-C_3N_4-O, which correspond to N—C—O bond and adsorbed O_2, respectively [19,26]. However, the N—C—O bond at 531.1 eV could not be detected in g-C_3N_4 thin sheets, which indicates the oxygen doping mainly occurred during photo-Fenton reaction and located at the g-C_3N_4 edge, which is consistent with FT-IR analysis (Fig. S2). To further eliminate possible other kinds of bonds, such as carbon vacancies, their deconvolutions of C1s XPS are shown in Fig. 4. It can be clearly observed there is two main peaks located at 284.6 and 288.1 eV, corresponding to characteristic CC and C—N—C bonds in g-C_3N_4. However, a distinctive peak located at 289.6 eV is found in the HS g-C_3N_4-O (Fig. 4c), which could be ascribed to oxygen atom substitute for nitrogen atom because of easy migration of electrons bound to oxygen.

The photocatalytic H_2 evolution over bulk g-C_3N_4, HS g-C_3N_4-O and g-C_3N_4 thin sheets was tested under simulated solar light using triethanolamine as sacrificial agent. As shown in Fig. 5a, the H_2 evolution rate of the bulk g-C_3N_4 is 70.65 μmol/h, while that of g-C_3N_4 thin sheets achieve to 122.56 μmol/h. It is believed that the increased H_2 evolution rate are associated with the improved electron transport and/or electronic band structure changes induced by quantum confinement effect in the thin sheets [12]. When further increased the surface area and doped with oxygen in HS g-C_3N_4-O, the H_2 evolution rate of the bulk g-C_3N_4 dramatically increase to 202.56 μmol/h and the evolution rate is quite stable under continuous irradiation of 26 h. The enhanced photocatalytic performance is further evaluated by decolorizating Rh.B under simulated solar light. As shown in Fig. 5b, complete decolorization of Rh.B over HS g-C_3N_4-O could be carried out within 50 min. However, the complete decolorizations of Rh.B over bulk g-C_3N_4 and g-C_3N_4 thin sheets need take 130 and 100 min under the same condition as the process for HS g-C_3N_4-O, respectively. These results demonstrate a significant enhancement in both photocatalytic H_2 generation and decolorizations of Rh.B using HS g-C_3N_4-O, the mechanism of which will be explained from the analysis of Fig. 6. As known, the semiconductor photocatalysis process is composed of the photoexcitation, the separation and transfer of photoinduced charge carriers, and the subsequent photocatalytic reaction. The photoexcitation primarily depends on the bandgap structure of the semiconductor. The UV–vis absorption spectra of bulk g-C_3N_4, g-C_3N_4 thin sheets and HS g-C_3N_4-O are shown in Fig. 6a. The band gap of photocatalysts could be determined by using the equation: $(\alpha h\nu)^n = A\ (h\nu - Eg)$, according to Fig. 6a, where α is the absorption coefficient, $h\nu$ is the light energy, A is a constant, Eg is the optical band gap energy, and n is equal to 1/2 for an indirect band gap (Fig. 6b). It is estimated that the indirect band gaps of the bulk g-C_3N_4, g-C_3N_4 thin sheets and HS g-C_3N_4-O are 2.62, 2.79 and 2.434 eV, respectively. It can be obviously seen that the band gap of g-C_3N_4 thin sheets is larger than bulk g-C_3N_4 due to the well-known quantum confinement effect by shifting the conduction and valence band edges in opposite directions [27]. After edge doping with oxygen, the band gap of HS g-C_3N_4-O is significantly reduced to 2.434 eV, suggesting more visible light harvesting capability. The result is reasonable because an oxygen atom owns one more electron than an N atom does, naturally, the substitution of N sites by O atoms would offer extra electrons in the HS g-C_3N_4-O in analogy to the Nb-doped TiO_2 system [28]. Subsequently, the extra electrons would be redistributed to their nearest carbon atoms and delocalized among the big π bonds of the g-C_3N_4, resulting in the formation of a defect-related state below the conduction band maximum (CBM) of the g-C_3N_4 [19]. The CBM could be estimated by Mott–Schottky plots, as shown in Fig. 6c. The flat band potentials (V_{fb}) of bulk g-C_3N_4, g-C_3N_4 thin sheets and HS g-C_3N_4-O samples are estimated to be 1.117, 1.175

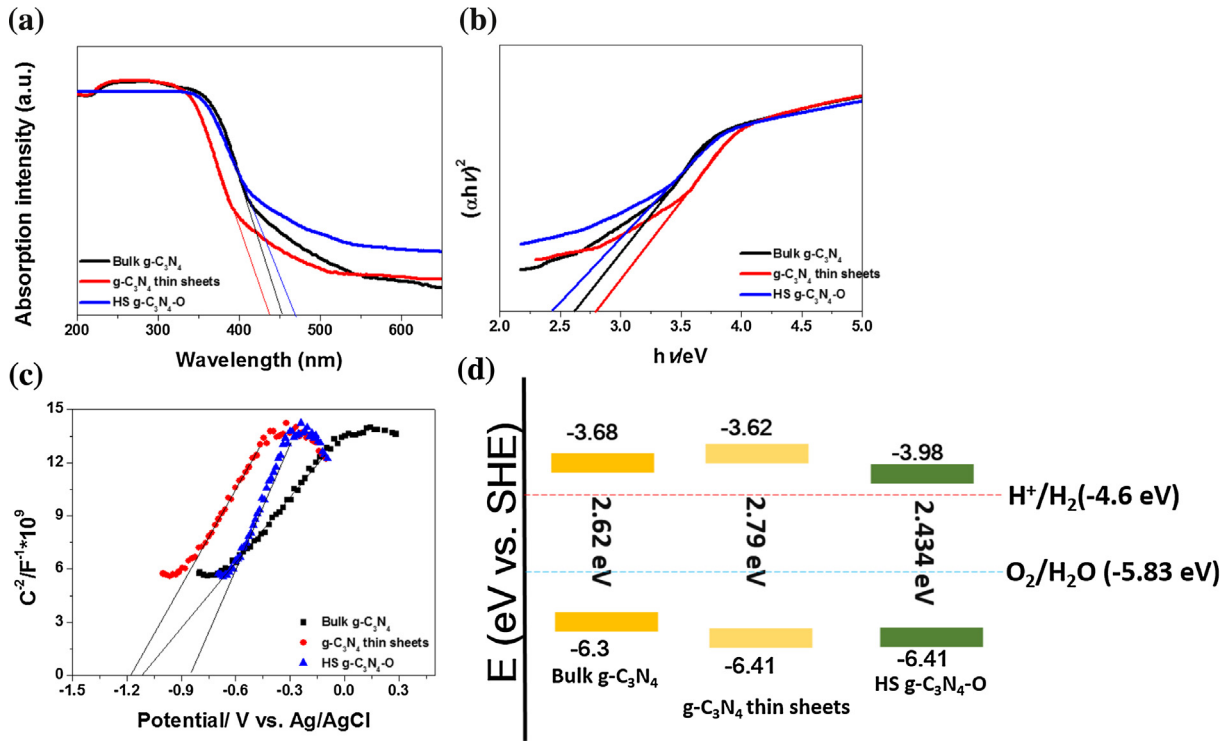

Fig. 6. (a) UV–vis absorption spectra of bulk g-C_3N_4, HS g-C_3N_4-O and g-C_3N_4 thin sheets. (b) The corresponding bandgap estimated by related curves of $(\alpha h\nu)^2$ vs photon energy plotted. (c) Mott–Schottky plots of bulk g-C_3N_4, HS g-C_3N_4-O and g-C_3N_4 thin sheets. (d) Comparison of electronic band structure of bulk g-C_3N_4, HS g-C_3N_4-O and g-C_3N_4 thin sheets.

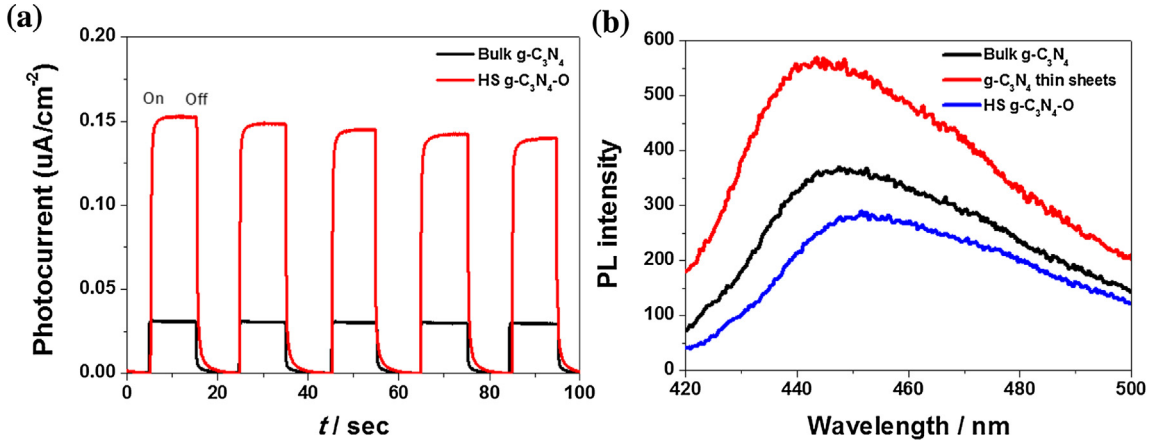

Fig. 7. (a) Photocurrent responses of bulk g-C_3N_4 and HS g-C_3N_4-O electrodes under visible light irradiation at 0.2 V vs Ag/AgCl in a 0.5 M Na_2SO_4 aqueous solution. (b) PL spectra of bulk g-C_3N_4, HS g-C_3N_4-O and g-C_3N_4 thin sheets by excited at 420 nm. (For interpretation of the references to color in the text, the reader is referred to the web version of this article.)

and 0.83 V, respectively. The V_{fb} could be converted to standard hydrogen electrode (SHE) by following the Eqs. (1)–(3):

$$E\ (\text{V vs RHE}) = V_{fb} + E^0{}_{Ag/AgCl} + 0.059 \times \text{pH} \quad (1)$$

$$E\ (\text{V vs SHE}) = E\ (\text{V vs RHE}) + 0.0592 \times \text{pH} \quad (2)$$

$$E\ (\text{eV}) = -4.6 - E\ (\text{V vs SHE}) \quad (3)$$

In the electron energy diagram with the unit eV, the vacuum energy is usually set to 0 eV, as a result, the V_{fb} vs SHE bulk g-C_3N_4, g-C_3N_4 thin sheets and HS g-C_3N_4-O samples are calculated to be −3.68, −3.62 and −3.98 eV, respectively. Assuming the difference between V_{fb} and CB minimum is negligible for n-type semiconductors [29], the determined V_{fb} can be approximated as the CB edge ($E_{cb} \approx V_{fb}$). Therefore, according to their band gap in Fig. 6b, these valance band maximum (VBM) was approximatively at −6.3, −6.41 and −6.41 eV respectively. Fig. 6d shows schematic energy level diagrams of the bulk g-C_3N_4, g-C_3N_4 thin sheets and HS g-C_3N_4-O in comparison with the potentials for water reduction and oxidation. It could be clearly seen that the VBM of HS g-C_3N_4-O has a similar position as that of g-C_3N_4 thin sheets, whereas the CBM of HS g-C_3N_4-O is 0.36 eV lower than that of g-C_3N_4 thin sheets. Therefore, it could be reasonably inferred that the oxygen edge doping significantly hybridizes atomic states by either the substitution of N sites by O atoms [10,19,30]. or structural distortion by the introduction of guest oxygen atoms [31]. As mentioned before, in addition to the light absorptivity, the separation and transfer of photo induced charge carriers act also important role on its photocatalytic activity. Photo luminescence (PL) spectra and photo

current response were therefore used to investigate the separation and transfer of photo induced charge carriers. As shown in Fig. 7a, the photoresponses for both bulk g-C_3N_4 and HS g-C_3N_4-O were reproducible during the repeated on/off cycles under visible light irradiation, suggesting efficient visible light harvesting. Moreover, the photocurrent of the HS g-C_3N_4-O electrode was about five times higher than that of the bulk g-C_3N_4 electrode, indicating a much more enhanced separation efficiency of photoinduced electrons and holes. Fig. 7b shows the PL spectra of the bulk g-C_3N_4, g-C_3N_4 thin sheets and HS g-C_3N_4-O excited by 420 nm at room temperature. The emission peak of the bulk g-C_3N_4 appears at ca. 446 nm, attributed to the band–band recombination of the charge carriers with emission photon energy equal to its bandgap energy. Significantly, the blue shift and raising intensity of emission peak for g-C_3N_4 thin sheets was due to shifting the conduction and valence band edges in opposite directions. Obviously, after oxygen edge doping, the emission peak was red-shifted with relative low intensity, suggesting that the recombination of electron–hole pairs might be effectively inhibited. According to above analyses and characterization, the improved photocatalytic activities for H_2 generation and Rh.B degradation could be ascribed to high surface area offering numerous catalytic sites, narrow band gap improving light harvesting and oxygen edge doping enabling more efficient charge generation and separation.

4. Conclusion

In summary, a facile process was developed to obtain holey structured g-C_3N_4 thin sheets with oxygen edge doping (HS g-C_3N_4-O) by photo-Fenton reaction. The holy structure efficiently increased surface area from 46 $m^2\ g^{-1}$ of bulk g-C_3N_4 to 348 $m^2\ g^{-1}$. The oxygen edge doping significantly improving light harvesting ability, and improves separation efficiency of the photoinduced charge carriers. As a results, the as-obtained HS g-C_3N_4-O presented high photocatalytic activities for H_2 evolution and Rh.B degradation. This study shows that this kind of noble-metal-free g-C_3N_4 has a great potential for solar energy conversion.

Acknowledgments

This work was supported by the National Science Foundation of China (NSFC) (Grant No. 21271010) and Shanghai Municipal Education Commission (No. 15ZZ088) and Science and Technology Commission of Shanghai Municipality (No. 14DZ2261000).

Appendix A. Supplementary data

Supplementary data associated with this article can be found, in the online version, at http://dx.doi.org/10.1016/j.apcatb.2015.11.030.

References

[1] K. Maeda, K. Teramura, D.L. Lu, T. Takata, N. Saito, Y. Inoue, K. Domen, Nature 440 (2006) 295.
[2] X.B. Chen, S.H. Shen, L.J. Guo, S.S. Mao, Chem. Rev. 110 (2010) 6503–6570.
[3] H. Tong, S. Ouyang, Y. Bi, N. Umezawa, M. Oshikiri, J. Ye, Adv. Mater. 24 (2012) 229–251.
[4] X. Wang, K. Maeda, A. Thomas, K. Takanabe, G. Xin, J.M. Carlsson, K. Domen, M. Antonietti, Nat. Mater. 8 (2008) 76–80.
[5] B. Yue, Q. Li, H. Iwai, T. Kako, J. Ye, Sci. Technol. Adv. Mater. 12 (2011) 034401.
[6] A.B. Jorge, D.J. Martin, M.T.S. Dhanoa, A.S. Rahman, N. Makwana, J. Tang, A. Sella, F. Cora, S. Firth, J.A. Darr, P.F. McMillan, J. Phys. Chem. C 117 (2013) 7178–7185.
[7] X. Wang, K. Maeda, X. Chen, K. Takanabe, K. Domen, Y. Hou, X. Fu, M. Antonietti, J. Am. Chem. Soc. 131 (2009) 1680–1681.
[8] Y. Wang, J.S. Zhang, X.C. Wang, M. Antonietti, H.R. Li, Angew. Chem. Int. Ed. 49 (2010) 3356–3359.
[9] Y.J. Zhang, T. Mori, J.H. Ye, M. Antonietti, J. Am. Chem. Soc. 132 (2010) 6294–6295.
[10] G. Liu, P. Niu, C.H. Sun, S.C. Smith, Z.G. Chen, G.Q. Lu, H.M. Cheng, J. Am. Chem. Soc. 132 (2010) 11642–11648.
[11] G.G. Zhang, M.W. Zhang, X.X. Ye, X.Q. Qiu, S. Lin, X.C. Wang, Adv. Mater. 26 (2014) 805–809.
[12] P. Niu, L.L. Zhang, G. Liu, H.M. Cheng, Adv. Funct. Mater. 22 (2012) 4763–4770.
[13] J.Y. Zhang, Y.H. Wang, J. Jin, J. Zhang, Z. Lin, F. Huang, J.G. Yu, ACS Appl. Mater. Interfaces 5 (2013) 10317–10324.
[14] L. Ge, F. Zuo, J.K. Liu, Q. Ma, C. Wang, D.Z. Sun, L. Bartels, P.Y. Feng, J. Phys. Chem. C 116 (2012) 13708–13714.
[15] C.J. Li, S.P. Wang, T. Wang, Y.J. Wei, P. Zhang, J.L. Gong, Small 10 (2014) 2783–2790.
[16] Y.L. Chen, J.H. Li, Z.H. Hong, B. Shen, B.Z. Lin, B.F. Gao, Phys. Chem. Chem. Phys. 16 (2014) 8106–8113.
[17] Q.J. Xiang, J.G. Yu, M. Jaroniec, J. Phys. Chem. C 115 (2011) 7355–7363.
[18] G.Z. Liao, S. Chen, X. Quan, H.T. Yu, H.M. Zhao, J. Mater. Chem. 22 (2012) 2721–2726.
[19] J.H. Li, B. Shen, Z.H. Hong, B.Z. Lin, B.F. Gao, Y.L. Chen, Chem. Commun. 48 (2012) 12017–12019.
[20] G.H. Dong, Z.H. Ai, L.Z. Zhang, RSC Adv. 4 (2014) 5553–5560.
[21] K. Ikehata, M.G. El-Din, J. Environ. Eng. Sci. 5 (2006) 81–135.
[22] J.G. Radich, P.V. Kamat, ACS Nano 7 (2013) 5546–5557.
[23] Y.X. Xu, Z.Y. Lin, X. Zhong, X.Q. Huang, N.O. Weiss, Y. Huang, X.F. Duan, Nat. Commun. 5 (2014) 4554.
[24] J.G. Yu, H.G. Yu, B. Cheng, M.H. Zhou, X.J. Zhao, J. Mol. Catal. A 253 (2006) 112–118.
[25] C.R. Clayton, Y.C. Lu, J. Electrochem. Soc. 133 (1986) 2465–2473.
[26] L.N. Bui, M. Thompson, N.B. McKeown, A.D. Romaschin, P.G. Kalman, Analyst 118 (1993) 463–474.
[27] A.P. Alivisatos, Science 271 (1996) 933–937.
[28] J.H. Lima, P. Murugan, N. Lakshminarasimhan, J.Y. Kim, J.S. Lee, S.H. Lee, W.Y. Choi, J. Catal. 310 (2014) 91–99.
[29] J. Premkumar, Chem. Mater. 16 (2004) 3980–3981.
[30] Z.F. Huang, J.J. Song, L. Pan, Z. Wang, X.Q. Zhang, J.J. Zou, W.B. Mi, X.W. Zhang, L. Wang, Nano Energy 12 (2015) 646–656.
[31] H. Wang, X.D. Zhang, J.F. Xie, J.J. Zhang, P. Ma, B.C. Pan, Y. Xi, Nanoscale 7 (2015) 5152–5156.